Electron beam deceleration measurements using the decelerator test beam line in the Compact Linear Collider test facility

R. L. Lillestøl,[1,2*] S. Döbert,[1] E. Adli,[2] and M. Olvegård[3]
[1]CERN, CH-1211 Geneva 23, Switzerland
[2]Department of Physics, University of Oslo, 0316 Oslo, Norway
[3]Department of Physics and Astronomy, Uppsala University, 75120 Uppsala, Sweden
(Received 29 October 2013; published 24 March 2014)

We discuss beam deceleration through a series of 12 power extraction and transfer structures, at the CLIC test facility 3 at CERN, as a proof-of-principle of the CLIC deceleration scheme. Up to 36% of the kinetic energy of an electron drive beam is extracted and converted to 12 GHz rf power. We look at the average and maximum energy loss of the particles, and compare them with simulations performed with the PLACET tracking code. The measured final energy is also compared to predictions based on the measured beam current and rf power in the structures. In the analysis we make use of the charge distribution form factor, taking into account the bunch length and the bunch phase. Finally, we look at the evolution of the transverse emittance with deceleration and compare the measured emittance with simulations.

DOI: 10.1103/PhysRevSTAB.17.031003 PACS numbers: 41.75.Ht, 29.27.−a, 29.20.Ej

I. INTRODUCTION

The proposed future e^+e^- collider CLIC [1] will use a two-beam scheme, in which an electron drive beam running in decelerators parallel to the main beam acts as a power source for accelerating the main beam to the final energy of 3 TeV. This allows a very high accelerating gradient for the main beam of 100 MV/m using normal conducting technology with a high efficiency.

Energy is extracted from the drive beam using power extraction and transfer structures (PETS), which are passive, periodically loaded microwave structures with a preferred synchronous mode at $\omega_{\mathrm{rf}}/2\pi = 12$ GHz [1]. The resonating wakefield in the PETS builds up constructively from the passing bunch train, which has a 12 GHz bunch frequency. The rf power travels down the structures with a group velocity of $0.46c$, where c is the speed of light and is extracted via output couplers. Finally, waveguides guide the power to the accelerating structures of the main beam for acceleration. The drive beam loses kinetic energy from the extraction in the PETS, and at the end of the decelerators the most decelerated particles will have lost 90% of their initial energy of 2.4 GeV. Due to the field buildup of the PETS, the produced rf power has a short transient at the start of the bunch train [2]. The beam also develops a large energy spread. The beam dynamics of a decelerated beam has previously been studied in detail for relativistic klystron two-beam accelerators in [3] for a lower beam energy than the CLIC drive beam will have.

An important challenge for CLIC is to transport the heavily decelerated drive beam, with its large energy spread, through the 1 km long decelerators. The transverse beam size will increase because of adiabatic undamping from the deceleration, and at the end of the decelerators the beam will fill a large part of the aperture. It is therefore important to ensure that the transverse phase space does not increase significantly due to other effects like higher-order modes in the PETS. The structures will be equipped with higher-order mode absorbers to counteract this. There is also a strict tolerance on quadrupole magnet misalignment, and advanced beam-based alignment schemes and precise alignment techniques will be needed.

At CERN, the CLIC test facility 3 was set up to verify and demonstrate key concepts of the CLIC scheme [4]. Most of the facility consists of a drive beam complex, where an electron beam is created, bunched, accelerated, and interleaved in a delay loop and a combiner ring, similar to the future CLIC machine. One of the main experiments is the decelerator test beam line (TBL), which is a prototype decelerator where the electron beam is decelerated through a series of PETS. The energy extracted in the TBL is measured and dissipated in rf loads. The main focus of the experiment is to demonstrate low-loss transport of a heavily decelerated beam, to benchmark PETS power production with theory, and to operate a small-scale decelerator.

For reference, a simulation of the particle energies at the end of the TBL is shown in Fig. 1, performed with the PLACET tracking code [5]. The simulation assumes nominal conditions with all PETS installed, where the most decelerated particles will have lost 55% of the initial energy of 150 MeV. The figure shows the high-energy transient at the

*reidar.lunde.lillestol@cern.ch

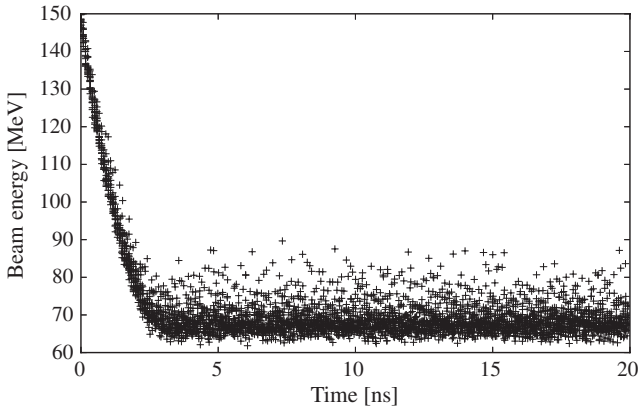

FIG. 1. Energies of simulated particles in the TBL from the PLACET tracking code. Nominal beam parameters were used in the simulation, and the plot shows the first 20 ns out of the 140 ns bunch train. At the start one can easily see the high-energy transient time that occurs due to the field buildup in the PETS.

beginning of the pulse, and a significant energy spread of 14% (FWHM) in the steady state. Particles of all energies, undergoing different levels of deceleration, must be transported to the end of the line.

In this paper we present a detailed analysis of the relation between drive beam parameters, power production, and energy loss. Some preliminary results were reported in [6]. We demonstrate that all aspects of the CLIC drive beam deceleration and rf power production are well understood. Key formulas are presented in Sec. II, and one parameter is elaborated on in Sec. III, with derivations of new equations. In Sec. IV we describe the experimental setup of the TBL. Finally we present the experimental results, focusing on deceleration results in Sec. V and the evolution of the transverse emittance in Sec. VI.

II. BEAM DECELERATION

The power P produced in a PETS at steady state is given by [2,7]

$$P = \frac{1}{4}(R'/Q)\frac{\omega_{\mathrm{rf}}}{v_g}L^2I^2F^2\{\lambda(z)\}\eta_\Omega^2, \tag{1}$$

where R'/Q is proportional to the structure impedance per meter, ω_{rf} the synchronous frequency, v_g the group velocity, L the structure length, I the beam current, η_Ω an ohmic loss factor, and $F\{\lambda(z)\}$ the charge distribution form factor. The parameters R'/Q, ω_{rf}, v_g, and η_Ω all refer to the preferred synchronous PETS mode used for power production. The charge distribution form factor will be discussed in detail in the next section.

The maximum energy loss of a steady-state particle in one PETS is equivalent to the peak voltage $\hat{V}$ seen by the particle in the structure,

$$\hat{V} = \frac{L}{2}\sqrt{\frac{(R'/Q)\omega_{\mathrm{rf}}}{v_g}P}. \tag{2}$$

Combining this with Eq. (1), the maximum energy loss can also be written

$$\hat{V} = \frac{L^2}{4}(R'/Q)\frac{\omega_{\mathrm{rf}}}{v_g}IF\{\lambda(z)\}\eta_\Omega. \tag{3}$$

We can further express the mean energy loss in one structure as

$$\langle V\rangle = \hat{V}F\{\lambda(z)\} = \frac{L^2}{4}(R'/Q)\frac{\omega_{\mathrm{rf}}}{v_g}IF^2\{\lambda(z)\}\eta_\Omega. \tag{4}$$

Using Eqs. (2)–(4), it is possible to predict the deceleration from either the form factor and the measured power, or from the form factor and the measured beam current.

It is vital to use a high average beam current in order to produce high power in accordance with Eq. (1). In CLIC, drive beam bunches are interleaved in one delay loop and two combiner rings, which together increase the bunch frequency and the average beam current by a factor of 24 while shortening the bunch train. After combination, the average beam current will be 101 A. The CTF3 has one delay loop and one combiner ring, which together can produce a maximum beam current of 28 A.

III. THE FORM FACTOR

We now turn our eyes to the charge distribution form factor $F\{\lambda(z)\}$ that appears in Eqs. (1)–(4), and derive an equation where the contributions from the bunch phase and the bunch lengths are separated. This is relevant for the CLIC scheme because of the complex bunch interleaving process which can result in systematic bunch phase errors. $F\{\lambda(z)\}$ will simply be referred to as "the form factor."

The power in a PETS depends on the wakefields from the last N_{b} bunches, where N_{b} is the number of bunches required for the field buildup in the structure that causes a transient as shown in Fig. 1. This number is given by

$$N_{\mathrm{b}} = Lf_{\mathrm{b}}\left(\frac{1}{v_g} - \frac{1}{c}\right), \tag{5}$$

where f_{b} is the bunch frequency.

At a given time we consider the longitudinal charge distribution $\lambda(z)$ of the last N_{b} bunches, and normalize it so that $\int_{-\infty}^{\infty}\lambda(z)dz = 1$. Then, the form factor is defined as the absolute value of its Fourier transform evaluated at the bunch frequency f_{b},

$$F\{\lambda(z)\} \equiv \left|\int_{-\infty}^{\infty}\lambda(z)e^{i2\pi f_{\mathrm{b}}z/c}\mathrm{d}z\right|, \tag{6}$$

and we have the constraint $0 \le F\{\lambda(z)\} \le 1$. The upper bound would apply for pointlike bunches that arrive with no deviation from the correct bunch frequency.

We write the total effective charge distribution as a sum over the charge distribution $\lambda_n(z)$ of each individual bunch, $\lambda(z) = \sum_{n=1}^{N_b} \lambda_n(z)$. The center of each of these bunches is defined as

$$z_n \equiv \frac{\int_{-\infty}^{\infty} z\lambda_n(z)\mathrm{d}z}{\int_{-\infty}^{\infty} \lambda_n(z)\mathrm{d}z}, \tag{7}$$

and we define a phase ϕ_n for each bunch as

$$\phi_n = \exp\left(\frac{i2\pi f_b z_n}{c}\right). \tag{8}$$

The form factor can then be written

$$\begin{aligned} F\{\lambda(z)\} &= \left| \int_{-\infty}^{\infty} \sum_{n=1}^{N_b} \lambda_n(z) \exp\left(\frac{i2\pi f_b z_n}{c}\right) \right. \\ &\quad \left. \times \exp\left[\frac{i2\pi f_b (z - z_n)}{c}\right] \mathrm{d}z \right| \\ &= \left| \int_{-\infty}^{\infty} \sum_{n=1}^{N_b} \lambda_n(z) e^{i\phi_n} e^{i\theta_n(z-z_n)} \mathrm{d}z \right|, \end{aligned} \tag{9}$$

where $\theta_n(z - z_n) = 2\pi f_b(z - z_n)/c$ is an interbunch phase relative to the bunch center.

By introducing a change of variables $z' = z - z_n$, we rewrite Eq. (9) as

$$\begin{aligned} F\{\lambda(z')\} &= \left| \int_{-\infty}^{\infty} \sum_{n=1}^{N_b} \lambda_n(z' + z_n) e^{i\phi_n} e^{i\theta_n(z')} \mathrm{d}z' \right| \\ &= \left| \int_{-\infty}^{\infty} \sum_{n=1}^{N_b} \lambda_0(z') e^{i\phi_n} e^{i\theta_0(z')} \mathrm{d}z' \right|, \end{aligned} \tag{10}$$

where in the last step we utilize a new function $\lambda_0(z') = \lambda_n(z' + z_n)$. Since $\lambda_n(z)$ is symmetric around z_n, the new function $\lambda_0(z')$ is symmetric around 0. If we consider equal bunch charge distributions, $\lambda_0(z')$ is not dependent on the bunch number n. In addition, the function $\theta_n(z')$ now has no dependence on n, and is renamed $\theta_0(z')$. Both $\lambda_0(z')$ and $\theta_0(z')$ can therefore be moved out of the summation. The bunch phase ϕ_n has no z' dependence, and can be taken out of the integral. Thus, we can separate Eq. (10) into

$$F\{\lambda(z')\} = \left| \left(\sum_{n=1}^{N_b} e^{i\phi_n} \right) \int_{-\infty}^{\infty} \lambda_0(z') e^{i\theta_0(z')} \mathrm{d}z' \right|. \tag{11}$$

We also assume that the charge distribution $\lambda_0(z')$ is an even function around 0 (a symmetric bunch) that is strictly decreasing when $|z'|$ moves away from zero,

$$\frac{\mathrm{d}}{\mathrm{d}z'} \lambda_0(z') < 0, \qquad z' > 0, \tag{12}$$

$$\frac{\mathrm{d}}{\mathrm{d}z'} \lambda_0(z') > 0, \qquad z' < 0. \tag{13}$$

If we also only consider relatively short bunches, i.e., that the charge distribution follows the criterion

$$\int_0^{c/4f_b} \lambda_0(z')\mathrm{d}z' \ge \int_{c/4f_b}^{3c/4f_b} \lambda_0(z')\mathrm{d}z', \tag{14}$$

the integral in Eq. (11) will be real and positive, and we can write

$$F\{\lambda(z')\} = \left| \sum_{n=1}^{N_b} e^{i\phi_n} \right| \times \int_{-\infty}^{\infty} \lambda_0(z') e^{i\theta_0(z')} \mathrm{d}z'. \tag{15}$$

The sum and the integral can be normalized separately by multiplying Eq. (15) with N_b/N_b,

$$\begin{aligned} F\{\lambda(z')\} &= \frac{1}{N_b} \left| \sum_{n=1}^{N_b} e^{i\phi_n} \right| N_b \int_{-\infty}^{\infty} \lambda_0(z') e^{i\theta_0(z')} \mathrm{d}z' \\ &\equiv \Phi(\{\phi_n\}) F_b\{\lambda_0(z')\}. \end{aligned} \tag{16}$$

Here we have introduced the functional

$$F_b\{\lambda_0(z')\} \equiv N_b \int_{-\infty}^{\infty} \lambda_0(z') e^{i\theta_0(z')} \mathrm{d}z' \tag{17}$$

which defines the single-bunch form factor, and the function

$$\Phi(\{\phi_n\}) \equiv \frac{1}{N_b} \left| \sum_{n=1}^{N_b} e^{i\phi_n} \right| \tag{18}$$

which defines the multibunch form factor. Because of normalization we have the following bounds,

$$0 \le F_b\{\lambda_0(z')\} \le 1, \tag{19}$$

$$0 \le \Phi(\{\phi_n\}) \le 1. \tag{20}$$

According to Eq. (18), the absolute bunch phase at a given time has no relevance for the absolute PETS power production, which only depends on the dynamic phase change over a time equal to the field buildup time. When the last N_b bunches have had the same bunch phase, the multibunch form factor will evaluate to 1. Any phase change will cause a form factor reduction, and consequently a lower power production and energy extraction.

For Gaussian bunch distributions we can further simplify the single-bunch form factor. Based on streak camera measurements in the TBL, an assumption of Gaussianity

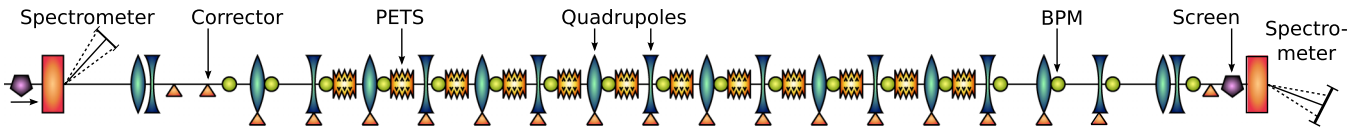

FIG. 2. The current TBL lattice. Quadrupole magnets are shown as blue lenses, dipole magnets as orange rectangles, corrector devices as orange triangles, BPMs as green circles, OTR screens as purple pentagons, and PETS as brown corrugated structures.

in the longitudinal distribution is reasonable. Consider a normalized Gaussian distribution around zero,

$$\lambda_0(z') = \frac{1}{N_\mathrm{b}\sqrt{2\pi}\sigma_z}\exp\left(-\frac{z'^2}{2\sigma_z^2}\right). \tag{21}$$

From numerical calculations we find that for the CLIC bunch frequency the condition in Eq. (14) is satisfied for $\sigma_z \leq 9.9$ mm. The single-bunch form factor in Eq. (17), by properties of the Fourier transform of a Gaussian, evaluates to

$$F_\mathrm{b}\{\lambda_0(z')\} = F_\mathrm{b}(\sigma_z) = \exp\left(-\frac{2\pi^2\sigma_z^2 f_\mathrm{b}^2}{c^2}\right). \tag{22}$$

From Eq. (22) we see the importance of having short bunches in the drive beam, to maximize the power production and energy extraction from Eqs. (1)–(4). In CLIC and in nominal CTF3 operation, the bunches are $\sigma_z = 1$ mm long.

IV. EXPERIMENTAL SETUP

In the following, we will describe the experimental equipment that make up the TBL. Similar to the CLIC decelerators, the TBL optics mainly consists of a FODO (focusing magnet, drift space, defocusing magnet, drift space) lattice. This was chosen to provide tight focusing in conditions of strong transverse wakes and because of the need for a large energy acceptance. The quadrupole focusing is tapered to provide constant focusing for the most decelerated particles, as proposed in [8]. The high-energy particles in the transient are then contained in the envelope of the low-energy particles. Normal operation uses a 90° phase advance per cell. The TBL lattice at the time of writing is shown in Fig. 2, and a selection of beam, lattice, and structure parameters is given in Table I.

Each quadrupole magnet in the FODO lattice is mounted on a mechanical mover, which can move the magnet horizontally and vertically with a precision of 5 μm. The movers were developed by CIEMAT, Madrid [9], and allow efficient beam steering and the use of beam-based alignment routines. The lattice also includes three conventional dipole corrector magnets.

TABLE I. Beam, lattice, and PETS structure parameters. Nominal parameters are given for both the TBL and one CLIC decelerator, in addition to currently achieved numbers for the TBL.

Symbol	Parameters	Current TBL	Nominal TBL	CLIC design
–	Total length of lattice [m]	40	40	≤ 1053
E_0	Initial energy [MeV]	120–125	150	2,370
E_min	Minimum final energy [MeV]	77–118	67	240
η_extr	Energy extraction, $(E_0 - E_\mathrm{min})/E_0$ [%]	6–36	55	90
σ_z	Bunch length, rms [mm]	1.0–2.5	1.0	1.0
–	Bunch charge [nC]	2.3	2.3	8.4
f_b	Bunch frequency [GHz]	1.499–11.994	11.994	11.994
–	Bunch train length [ns]	140–1120	140	244
I	Beam current [A]	3.5–22	28	101
$\varepsilon_{N_{x,y}}$	Initial norm. transverse emittances, rms [μm]	150–500	150	150
–	Number of PETS [–]	12	16	1492
–	Vacuum chamber inner radius [mm]	11.5	11.5	11.5
–	Repetition rate [Hz]	0.83–1.67	0.83–5.0	50
$\omega_\mathrm{rf}/2\pi$	Synch. mode frequency [GHz]	11.994	11.994	11.994
R'/Q	Synch. mode impedance per meter [linac-Ω/m]	2,222	2,222	2,290
v_g	Synch. mode group velocity [c]	0.46	0.46	0.45
η_Ω	Synch. mode ohmic loss factor [–]	0.985	0.985	0.996
L	PETS length [m]	0.8	0.8	0.235
P	Power production per PETS [MW]	2–70	135	134
$\hat{V}$	Max. deceleration per PETS [MeV]	0.6–3.3	5.2	1.45
N_b	Bunches required for field build-up [–]	37	37	10

The TBL has space between the quadrupoles for 16 PETS, of which 12 are currently installed. Three structures were constructed by CIEMAT [10,11] and the other nine were constructed at CERN. Since the nominal CTF3 drive beam current is around 1/4 of the CLIC drive beam current, the PETS are four times longer for compensation, and can produce roughly the same amount of rf power in accordance with Eq. (1). Each PETS is placed in a vacuum tank with water cooling, to avoid frequency shifts due to thermal deformation. One of the installed PETS tanks is shown in Fig. 3. All of the structures are equipped with higher-order mode absorbers made of silicon carbide, to damp any deflecting higher-order modes which can induce beam loss.

At the downstream side of each PETS, an output coupler guides the field into two waveguide arms. One arm from each structure is connected to readout electronics through a directional coupler and an attenuation chain for measuring the produced power. Most of the power is not used for measurements via the directional coupler but is dissipated in water-cooled loads. In case some power would be reflected by the load, this can also be measured. Since the power amplitude is too high to be measured directly, the power is attenuated by approximately 90 dB before entering the electronics. This includes the directional coupler, attenuators, and cables. The attenuation chain must be calibrated piecewise, and this can lead to a large systematic error for the power amplitude. We estimate a power calibration error of up to 20%, which corresponds to an attenuation error of 0.8 dB over the whole measurement chain. Note that this describes a constant attenuation error of the whole signal, such that the signal shape should be unaffected. The power amplitude from each PETS is measured with Schottky diodes. In addition, one PETS is measured with IQ (in-phase/quadrature-phase) demodulators that also give information about the rf phase.

The beam position monitors (BPMs) in the TBL are a scaled and revised version of those in the CTF3 drive beam linac [12]. They were designed and manufactured by IFIC Valencia and UPC Barcelona, and are inductive pickup wall current monitors that are also used for intensity diagnostics. The major error contribution in the intensity measurements is the resolution of the 192 MHz digitizers [13], which is constant and therefore relatively larger at lower beam currents.

The beam current entering the TBL can range from 3.5 A to 28 A. This is because the CTF3 contains one delay loop that can interleave bunches by a factor of two, and one combiner ring that can interleave bunches by a factor of four. When both of these are used, the initial bunch frequency of 1.5 GHz and the average intensity of 3.5 A are multiplied by a factor of 8. During operation it is also possible to bypass either or both of these, which gives access to the large intensity span. This allows TBL operation with different amounts of deceleration, since the beam current affects the deceleration linearly according to Eqs. (2)–(4).

In order to measure the energy of the decelerated beam, there is one spectrometer at the beginning and another at the end of the TBL. The spectrometer at the end of the line is a segmented dump that consists of 32 tungsten segments, which allows for time-resolved, single-shot spectrometry with a resolution of 1% [14–16]. The spectrometer at the beginning of the line is of a simpler type and is equipped with a single slit, which provides time-resolved spectrometry with a scan.

Optical transition radiation (OTR) screens are used for monitoring the transverse beam distribution, and are used in emittance measurements. One of these screens is placed just before the dipole magnet at the entry to the experiment, while another is placed after the decelerator FODO lattice, as shown in Fig. 2. These screens are inserted into the vacuum pipe when measurements are needed and are imaged by charge-coupled device (CCD) cameras. Finally, a streak camera imaging the OTR screen at the beginning of the line can provide information about the bunch length and bunch spacing. The performance of the OTR screens is documented in [14,17].

Compared to the future CLIC decelerators, the TBL experiment starts with a lower incoming energy and usually a higher emittance in both the longitudinal and the transverse planes. In addition, the TBL suffers from beam jitter originating from the CTF3, even though this is under improvement [18]. Thus, the TBL experiment is considered more challenging than the CLIC case.

Some of the nominal beam parameters in Table I have not yet been reached, mainly because of upstream beam losses originating from the combination process.

V. DECELERATION RESULTS

We focus primarily on measurements where the CTF3 was set up for a factor of 4 bunch combination, by utilizing the CTF3 combiner ring and bypassing the delay loop. This gave an average beam current of 13.5 A during 280 ns long bunch trains. The measured incoming energy was $E_0 = 123.5$ MeV with an energy spread of 3.0% FWHM. The mean energy was lower than the nominal value in Table I because of two klystrons in the CTF3 linac that are not in operation. A data set collected over 60 consecutive pulses was used for the analysis.

The transmission along a decelerator line affects the possible deceleration and energy extraction because of the change in effective beam current. The transmission in the TBL is normally above 90%. The incoming beam current for the data set was 14.0 A and the outgoing was 13.2 A, resulting in a 94% transmission. The systematic error on the intensity measurement, dependent on the intensity level, was estimated to be 2%. Within this error the beam losses were spread fairly evenly over the beamline.

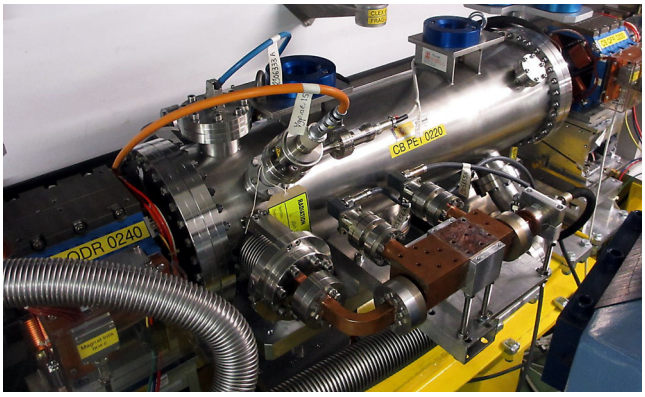

FIG. 3. One of the installed PETS tanks, which keeps the structure in a vacuum. In the front, one can see a waveguide arm, where the rf power is coupled out, measured, and dissipated in a load.

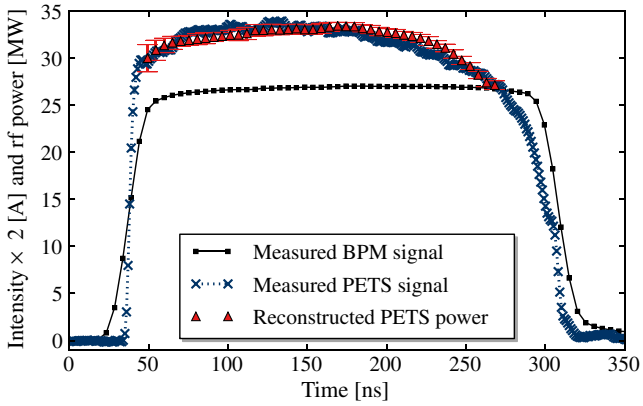

FIG. 4. Measured beam current and RF power for one BPM and one PETS. The beam current has been multiplied by a factor of 2. The shape of the produced power pulse is somewhat different from the beam current pulse, which can be explained by a change in the form factor over the pulse. A reconstruction from the BPM signal and the multibunch form factor based on Eqs. (1), (16), (18), and the signal in Fig. 5 is shown with red triangles.

The normalized horizontal emittance was measured to 330 μm instead of the nominal 150 μm. This blowup of the transverse phase space is believed to originate from a horizontal mismatch of the bunch combination, since a few distinct beam spots were visible on the OTR screens. By using the relation $\sigma_{x,y} = \sqrt{\varepsilon_{x,y}\beta_{x,y}}$ that relates the transverse beam size to the emittance and the beta function, the maximum $3\sigma_x$ beam size was 8.3 mm (the average size was 5.8 mm). Comparing this with the aperture of 11.5 mm, and taking into account the orbit which had an rms offset of 1.3 mm, we can expect that some scraping occurred which could account for the 6% beam loss. In addition, in the case of a nonperfect bunch combination the different beamlets may have had slightly different trajectories that were not shown by the BPM signal averages.

Figure 4 compares the signal from one PETS and the closest BPM, taken from the middle of the beamline. The beam current was almost constant along the pulse, with a rise-time dominated by the bandwidth of the electronics. The PETS rf power has a different and rounder shape. Since the only free parameter for the power production other than the beam current is the form factor,[1] we infer that there was a change of the bunch phase and/or the bunch length over the pulse, originating upstream.

Bunch length measurements were unavailable on the day of measurement, but we analyze the RF phase from the first PETS and calculate a multibunch form factor. The phase measurement from the combined beam cannot be used directly because there can be large bunch-to-bunch phase jumps from the combination, and the sampling frequency of the IQ demodulators is lower than the bunch frequency, which violates the Nyquist-Shannon sampling theorem. Instead we look at the phase from an uncombined beam (which should be smoother from bunch to bunch), measured for the same run at a different time. The 12 GHz phase as measured in the PETS is shown in Fig. 5. To construct a multibunch form factor, the raw 12 GHz phase measurement was first converted to $f_b = 3$ GHz phase, and interpolated to the same sample rate as the bunch frequency. The samples were then reshuffled to simulate a factor of 4 bunch combination in the combiner ring, and the phase was converted back to 12 GHz. Finally, a multibunch form factor was constructed where each sample was based on N_b samples from the calculated phase and Eq. (18). The resulting combined multibunch form factor was then resampled for use together with the BPM or the PETS signal. In Fig. 4 we show a reconstructed power signal based on the beam current squared and the multibunch form

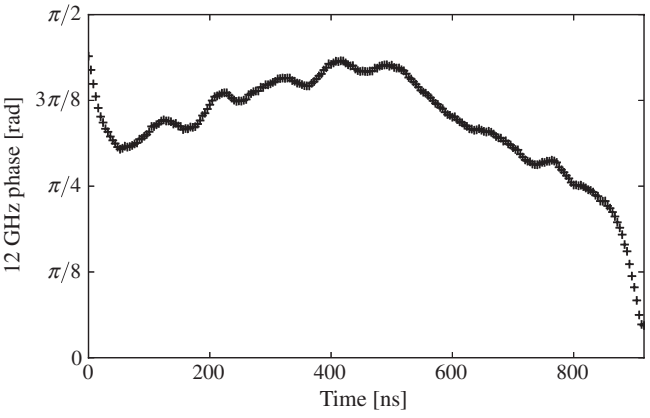

FIG. 5. 12 GHz phase measured in a PETS for an uncombined beam, which itself has a 3 GHz bunch structure and a longer bunch train than the combined beam.

[1]There is also a possibility of pulse shortening due to rf breakdowns in the PETS, however the breakdown rate is negligible at the measured power level, which is 1/4 of the nominal value.

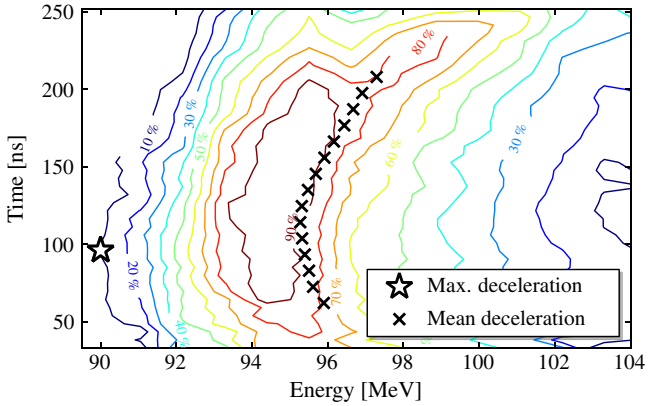

FIG. 6. Measured energy spectrum along the pulse at the end of the TBL for a beam current of 13.5 A. The contour lines show 10% increments of the maximum value of the signal, and the energy changes slightly along the pulse. The star shows the point with the most decelerated particles, while the crosses show the mean energies.

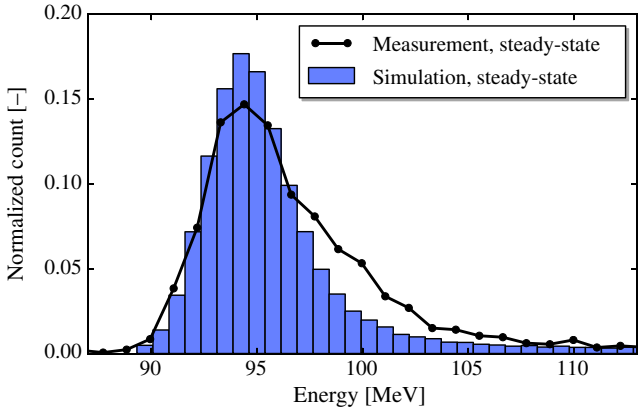

FIG. 7. The measured energy spectrum at the time instant with the most decelerated particles in Fig. 6. In addition, we show a simulated steady-state energy profile from PLACET for a form factor of $F\{\lambda(z)\} = 0.95$.

factor squared with Eq. (1). We see that the multibunch form factor to a large extent explains the different shape of the power signal. It is important to keep in mind that the significant phase change over the pulse is an artifact from the CTF3 machine, which is not built to have the same stability as CLIC.

The measured energy spectrum at the end of the TBL is shown in Fig. 6. The ordinate shows the time along the pulse, and we see that the energy changes slightly. The shape is similar to the PETS power in Fig. 4, as expected from the change in form factor. The contour lines indicate 10% increments of the signal compared to its maximum value. For finding the energy of the most decelerated particles, we define a threshold of 10% of the maximum signal. Close to the start of the pulse, this occurs at an energy of $E_{\mathrm{min}} = 90.0$ MeV. Expressing the total energy extraction as $\eta_{\mathrm{extr}} = (E_0 - E_{\mathrm{min}})/E_0$, we arrive at a maximum deceleration of $\eta_{\mathrm{extr}} = 27\%$.

Simulations of the TBL are regularly performed with the tracking code PLACET for comparing measurements with theory. PLACET simulates both single-bunch and multibunch wakefields and therefore provides a precise model of the beam energy spread. In Fig. 7, simulation results are shown where we used the measured input parameters taken together with the analyzed data set (i.e., an incoming energy of 123.5 MeV, 13.5 A beam current, 3.0% energy spread, and transverse parameters). In the same figure we have also plotted the measured energy profile at the time instant coinciding with the maximum deceleration, indicated by the star in Fig. 6. The bunch length had to be estimated in the simulation, because a streak camera measurement was unavailable during the run. For a form factor of $F\{\lambda(z)\} = 0.95$ in the simulation, we achieve a good agreement between simulation and measurement. Since the calculated multibunch form factor at this time instant was $\Phi(\{\phi_n\}) = 0.98$, by assuming Gaussian bunches we infer from Eq. (16) that the single-bunch form factor must have been $F_{\mathrm{b}}(\sigma_z) = 0.97$, corresponding to bunch lengths of $\sigma_z = 1.0$ mm. In Fig. 7 the measurement has a slightly different shape than the simulation because of an artifact in the incoming energy distribution that propagated down the beamline and that could not be reproduced in simulations. Note that the measured energy spread can be slightly overestimated due to beam scattering in the target and exit window close to the spectrometer [14], but according to simulations this overestimation is less than 1% in our case.

We next correlate the measured deceleration with that predicted from theory, and focus on the average deceleration indicated by crosses in Fig. 6. This is done for both the measured beam current and the PETS rf power, using Eqs. (2)–(4). The predicted deceleration from all individual BPM or PETS signals are added together and subtracted from the incoming energy. Our procedure for fitting the two predictions with the spectrometer measurement follows. (i) Fit the predicted deceleration from the beam current to the spectrometer measurement using Eq. (4) because the only free parameter that relates them is the form factor. The calculated multibunch form factor used for Fig. 4 is used, and a constant single-bunch form factor is chosen as an empirically derived scaling factor. Both form factor contributions are applied with Eq. (16). (ii) Fit the predicted deceleration from the PETS power with Eqs. (2) and (4) to the other two curves because this has a large scaling uncertainty from calibration errors, as described earlier. The same form factors $\Phi(\{\phi_n\})$ and $F_{\mathrm{b}}\{\lambda_0(z')\}$ are used, and a global scaling of the power amplitudes is used to estimate calibration errors. The scaling is applied before the square root in Eq. (2) is applied.

With this procedure, we arrive at a single-bunch form factor of $F_{\mathrm{b}}\{\lambda_0(z')\} = 0.96$. The rf power amplitudes need to be increased by 5%, and this is well within the expected

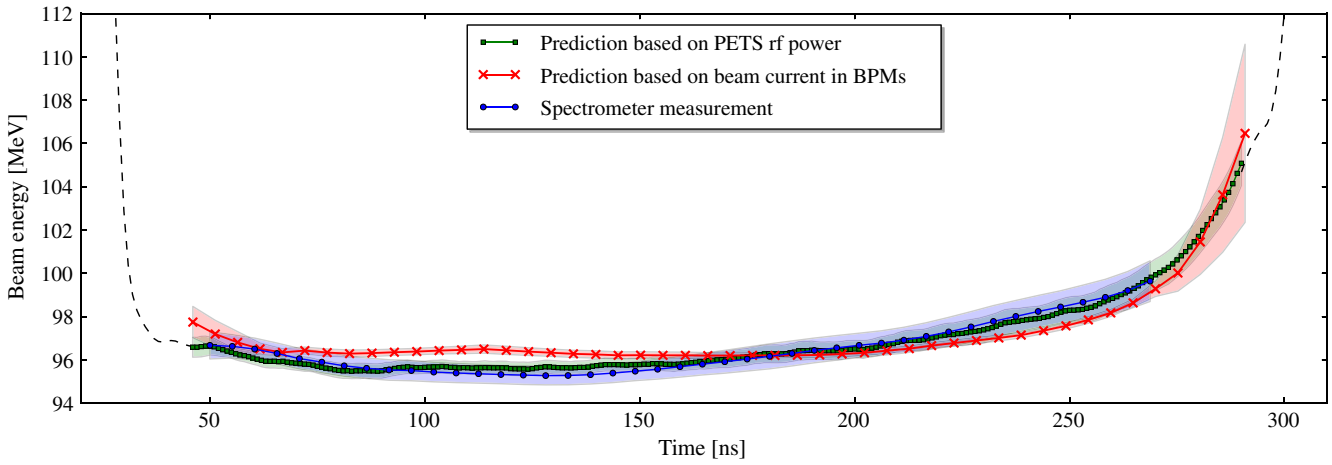

FIG. 8. Comparison between measured mean deceleration and deceleration predicted from measured beam current and PETS rf power. The curves with markers represent the average values over the data series, while the corresponding colored bands show the standard deviations. The predictions are only shown where the multibunch form factor could be calculated. Outside of this, we show the remaining signal based on the PETS rf power for reference, as a black stapled line.

uncertainty of the rf calibration. The results are shown in Fig. 8, which shows the average signals over the data series along with their standard deviations. Reliable phase information was only available in the steady-state part of the pulse, and this limits the area where the multibunch form factor can be applied. For reference we have also plotted the remaining prediction from the PETS power by using the $\Phi(\{\phi_n\})$ end-range values as guidelines for the pulse edges. The prediction based on the beam current has some small deviations from the other curves, and this can possibly be attributed to a small change in the bunch length, since our analysis uses a constant single-bunch form factor and the BPM signals are the only measurements that are not directly affected by the form factor. Note that the estimated single-bunch form factor $F_b\{\lambda_0(z')\} = 0.96$ is lower than the value obtained from the analysis in Fig. 7. This is because the latter describes a local form factor at close to the 100 ns mark in Figs. 6 and 8, where the bunch length may have been slightly shorter than the average value. Note also that the 6% beam loss mentioned earlier not only affects the BPM signals, but also the possible deceleration and the PETS rf power, such that it should not cause any discrepancy between the three signals.

As described earlier the CTF3 machine can be set up for different bunch combination schemes, and we can study how this affects the deceleration. Using the combiner ring only, the machine was set up for bunch combination with factors of 2, 3, and 4, and in addition we used the uncombined beam. This resulted in beam currents ranging from 3.5 to 13.5 A delivered to the TBL. At each setting 60 pulses were recorded, including the already analyzed data set. The bunch combination of a factor of 3 was set up twice

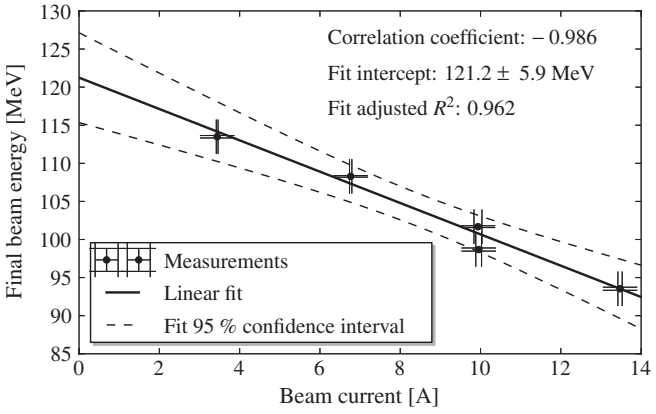

FIG. 9. Measured final energy at different beam currents and levels of deceleration. The intercept derived from a linear fit estimates what the final energy would be without deceleration.

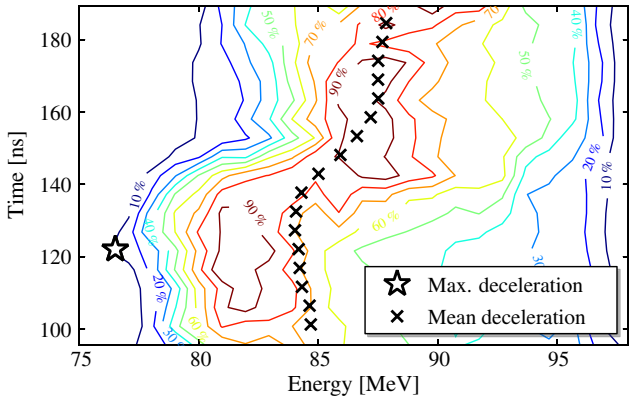

FIG. 10. Measured energy spectrum along the pulse at the end of the TBL, for 21.4 A beam current. The contour lines show 10% increments of the maximum value of the signal, and there is a step in the measured energy because of a change in the form factor. The star shows the point with the most decelerated particles, while the crosses show the mean energies.

due to instabilities during the first try. The resulting mean energies measured at the end of the TBL are shown in Fig. 9. The correlation coefficient between beam current and energy is −0.986. A linear fit was performed on the data, where the intercept was 121.2 MeV. This can be compared to the measured incoming energy of $E_0 =$ 123.5 MeV because it estimates the final energy without deceleration, something that is not possible to measure in practice. However, the intercept has a large uncertainty because the fit is extrapolated outside the measurement range. This is illustrated by the 95% confidence interval of the fit, which is shown with stapled lines in Fig. 9.

The maximum deceleration measured in the TBL was obtained during another run with an average beam current of 21.4 A and an incoming energy of 120 MeV, and amounts to 36%. Both the delay loop and the combiner ring were utilized, and the energy spectrum at the end of the line is shown in Fig. 10.

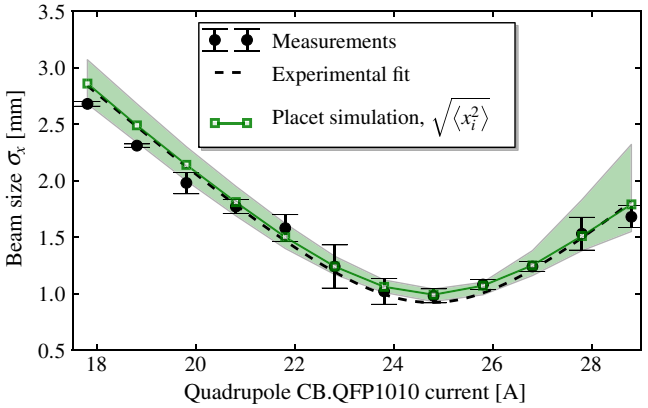

FIG. 11. Measured and simulated horizontal quadrupole scan at the end of the TBL. The measurement is an average of four quadrupole scans, and a parabola was fitted to the data. The curve for the simulations has a green band representing the uncertainty in the Twiss parameters and emittance measured at the beginning of the beamline.

VI. TRANSVERSE EMITTANCE

For CLIC, it is vital to know that the drive beam can be transported through the 1 km decelerators, even with heavy deceleration and a large energy spread. Deceleration will cause the transverse beam size to increase significantly from adiabatic undamping, since the energy is reduced by 90%.

In the TBL case, for a perfect machine at nominal conditions, the $3\sigma_{x,y}$ beam size will grow to 2/3 of the aperture [2] and the TBL is therefore a good test bench for the future machine. An important part of the experiment is therefore to study the evolution of the transverse emittance with deceleration.

In the TBL the transverse emittance is measured using quadrupole scans, in which the strength of one quadrupole magnet in a doublet is varied and the beam size is measured on a downstream OTR screen. A parabola is fitted to the resulting beam waist, and this gives information about the transverse emittances and the Twiss parameters. Instead of comparing single numbers for the emittance before and after deceleration, we have chosen another method that should be more meaningful. First, a number of quadrupole scans are performed at the beginning of the line, and numbers are averaged to find estimates of the emittances and Twiss parameters. The estimations are then used as input to a simulation code, in our case PLACET. A quadrupole scan is simulated at the end of the line, by varying the quadrupole strength of one magnet in the doublet in the simulation code. For the beam size we use the rms of the transverse particle distribution. Finally, a number of quadrupole scans are performed at the end of the line, and numbers are again averaged to find estimates that can be compared with simulations. If the normalized transverse emittances remain constant through the line, the beam waist should be the same in measurements and simulations at the end, and any deviations can be explained from the emittance or the Twiss parameters.

For technical reasons we have only been able to perform the experiment for the horizontal emittance, and for this we carried out three scans at the beginning of the line and four at the end. The measurements were performed during the same run as most of the results in Sec. V, with 13.5 A beam current and 27% deceleration. The average beam size measurements at the end of the line are shown with error bars in Fig. 11, and a parabolic fit to the data is shown with a black dashed curve.

Beam sizes obtained from simulations with PLACET are shown with a green line with squares, and this line is very close to the experimental fit. This is a strong indication that the normalized emittance was constant at 330 μm through the line. At the beginning of the line there was a certain spread in the measured parameters from the quadrupole scan, because of uncertainty in the individual beam size measurements and small differences between the three scans. We therefore also ran a scan of simulations with different parameters based on the error bars at the beginning of the line. The resulting spread in the simulated beam size at the end is shown with a light green band in Fig. 11.

For a beam with a large energy spread such as a drive beam, chromaticity affects the beam size measured during quadrupole scans as described in [19]. In the TBL with nominal conditions, chromaticity contributes a 20% error to the measured emittance [14], although this error can easily be corrected [19]. For the conditions here with less deceleration and consequently a lower final energy spread, the emittance error is significantly smaller and was estimated to 1.7%. Both measurement errors given here were found with a numerical method that did not use the thin-lens simplification from [19]. However, an assumption was made in the analysis that the beam arrives at the scanning

quadrupoles with no correlation between momentum and transverse beam position. In the PLACET simulations, chromatic effects are fully taken into account.

When including errors we see an excellent agreement between measurements and simulations, which means that the change in geometrical emittance can be attributed to adiabatic undamping alone.

VII. CONCLUSIONS

We have studied beam deceleration through a line of 12 PETS structures. At an average beam current of 13.5 A, the most decelerated particles experienced 27% deceleration. The measurements agreed well with simulations when a form factor of $F\{\lambda(z)\} = 0.95$ was used in the simulation code. We also correlated the spectrometer measurements with predicted deceleration based on the beam current and the power production in PETS. A multibunch form factor was calculated based on the PETS rf phase, and when this was used together with an estimated value of the single-bunch form factor we saw a good agreement, within the expected errors of the measurements. The maximum deceleration measured in the TBL at the time of writing amounts to 36%.

We also investigated the evolution of the horizontal emittance with deceleration. Quadrupole scans performed before and after deceleration were compared with particle tracking simulations, and there was an excellent agreement between measurements and simulations.

The deceleration experiments with the test beam line in the CTF3 are meant to validate the design of the CLIC decelerators. The presented results show that all relevant aspects of the beam deceleration and power production have been measured and agree well with theoretical predictions. The highest possible beam current and deceleration in the CTF3 have not been achieved, yet we consider the theoretical models used to design the CLIC decelerators as validated.

ACKNOWLEDGMENTS

We want to acknowledge the CTF3 operations team—F. Tecker, P. Skowronski, R. Corsini, T. Persson, B. Constance, D. Gamba, and J. Quirante—for setting up quality beams, aiding the TBL experiment, and making the most out of the machine. Furthermore, we want to thank our Spanish collaborators in CIEMAT, IFIC, and UPC for the design and construction of important experimental equipment. Finally, we acknowledge K. Sjøbæk, G. Sterbini, I. Syratchev, and A. Bell for fruitful discussions.

[1] M. Aicheler, P. Burrows, M. Draper, T. Garvey, P. Lebrun, K. Peach, N. Phinney, H. Schmickler, D. Schulte, and N. Toge, *A Multi-TeV Linear Collider Based on CLIC Technology: CLIC Conceptual Design Report* (CERN, Geneva, 2012).

[2] E. Adli, Ph.D. thesis, Oslo University, 2009 [http://cds.cern.ch/record/1239173].

[3] S. M. Lidia, in Phys. Rev. ST Accel. Beams **4**, 041001 (2001).

[4] G. Geschonke *et al.* (The CLIC Study Team), CTF3 Design Report No. CERN/PS-2002-008 (RF), 2002 [http://cds.cern.ch/record/559331].

[5] The PLACET tracking code, online at https://savannah.cern.ch/projects/placet/.

[6] R. L. Lillestol, S. Doebert, M. Olvegaard and E. Adli, in *Proceedings of the 4th International Particle Accelerator Conference, IPAC-2013, Shanghai, China, 2013* (JACoW, Shanghai, China, 2013).

[7] E. Adli, R. Ruber, V. Ziemann, R. Corsini, A. Dubrovskiy and I. Syratchev, Phys. Rev. ST Accel. Beams **14**, 081001 (2011).

[8] J. A. Riche, CERN Report No. CLIC-Note-266, 1994 [http://cds.cern.ch/record/275691].

[9] F. Toral *et al.*, in *11th Proceedings of the European Particle Accelerator Conference, Genoa, 2008* (EPS-AG, Genoa, Italy, 2008).

[10] D. Carrillo *et al.*, in *11th Proceedings of the European Particle Accelerator Conference, Genoa, 2008* (EPS-AG, Genoa, Italy, 2008).

[11] F. Toral *et al.*, in *Proceedings of the International Particle Accelerator Conference, Kyoto, Japan* (ICR, Kyoto, 2010).

[12] J. J. García Garrigós, M.Sc. thesis, Universidad Politecnica de Valencia, 2008 [http://cds.cern.ch/record/1164156].

[13] J. J. García Garrigós, Ph.D. thesis, Universidad Politécnica de Valéncia, 2013 [http://riunet.upv.es/handle/10251/34327].

[14] M. Olvegård *et al.*, Phys. Rev. ST Accel. Beams **16**, 082802 (2013).

[15] M. Olvegård *et al.*, Nucl. Instrum. Methods Phys. Res., Sect. A **683**, 29 (2012).

[16] M. Olvegård *et al.*, in *Proceedings of the International Particle Accelerator Conference, Kyoto, Japan* (ICR, Kyoto, 2010).

[17] M. Olvegård, B. Bolzon, E. Bravin, S. Burger, A. Dabrowski, T. Lefèvre, and C. P. Welsch, in *Proceedings of the 10th European Workshop on Beam Diagnostics and Instrumentation for Particle Accelerators, Hamburg, Germany, 2011* (DESY, Hamburg, 2011).

[18] T. Persson, P. Skowronski, and R. Corsini, Nucl. Instrum. Methods Phys. Res., Sect. A **735**, 152 (2014).

[19] M. Olvegård and V. Ziemann, Nucl. Instrum. Methods Phys. Res., Sect. A **707**, 114 (2013).